



Regularization and error characterization of GRACE mascons

B. D. Loomis¹ · S. B. Luthcke¹ · T. J. Sabaka¹

Received: 16 April 2018 / Accepted: 16 March 2019 / Published online: 15 April 2019

© This is a U.S. government work and its text is not subject to copyright protection in the United States; however, its text may be subject to foreign copyright protection 2019

Abstract

We present a new global time-variable gravity mascon solution derived from Gravity Recovery and Climate Experiment (GRACE) Level 1B data. The new product from the NASA Goddard Space Flight Center (GSFC) results from a novel approach that combines an iterative solution strategy with geographical binning of inter-satellite range-acceleration residuals in the construction of time-dependent regularization matrices applied in the inversion of mascon parameters. This estimation strategy is intentionally conservative as it seeks to maximize the role of the GRACE measurements on the final solution while minimizing the influence of the regularization design process. We fully reprocess the Level 1B data in the presence of the final mascon solution to generate true post-fit inter-satellite residuals, which are utilized to confirm solution convergence and to validate the mascon noise uncertainties. We also present the mathematical case that regularized mascon solutions are biased, and that this bias, or leakage, must be combined with the estimated noise variance to accurately assess total mascon uncertainties. The estimated leakage errors are determined from the monthly resolution operators. We present a simple approach to compute the total uncertainty for both individual mascon and regional analysis of the GSFC mascon product, and validate the results in comparison with independent mascon solutions and calibrated Stokes uncertainties. Lastly, we present the new solution and uncertainties with global analyses of the mass trends and annual amplitudes, and compute updated trends for the global ocean, and the respective contributions of the Greenland Ice Sheet, Antarctic Ice Sheet, Gulf of Alaska, and terrestrial water storage. This analysis highlights the successful closure of the global mean sea level budget, that is, the sum of global ocean mass from the GSFC mascons and the steric component from Argo floats agrees well with the total determined from sea surface altimetry.

Keywords GRACE · Time-variable gravity · Mascons · Range-acceleration · Regularization · Model resolution · Estimator bias

1 Introduction

The GRACE satellite mission monitored the temporal variability of the global gravity field with unprecedented accuracy for ~ 15 years, enabling new research and discoveries in the hydrologic, oceanographic, atmospheric, cryospheric, and solid Earth sciences. The accuracy of GRACE-derived time-variable gravity (TVG) solutions has improved over the course of the mission as the data processing and parameter estimation strategies have matured. Of primary importance in recent years has been the emergence of global mascon solutions as an alternative TVG product to the unconstrained

Stokes coefficients (Wahr et al. 1998), which were relied upon for the first decade of the mission. Mascon estimation from the GRACE Level 1B data was first done regionally (Rowlands et al. 2005; Luthcke et al. 2006, 2008) before being expanded to various global parameterizations (Sabaka et al. 2010; Luthcke et al. 2013; Watkins et al. 2015; Save et al. 2016). These mascon products have the important advantage of applying regularization in the least-squares gravity inversion, thus optimally combining the full noise and signal covariances (Sabaka et al. 2010). The most important design consideration for mascon estimation is the signal covariance, for which different strategies have emerged among the different GRACE processing centers that produce them.

Here, we present the new generation of NASA GSFC global mascon solutions, which advances the solutions presented in Luthcke et al. (2013). We estimate the same set of 41,168 1-arc-degree mascon cells as in the original solution

✉ B. D. Loomis
bryant.d.loomis@nasa.gov

¹ Geodesy and Geophysics Laboratory, NASA Goddard Space Flight Center, Greenbelt, MD, USA

(mascons have 1-degree latitude span, while the longitude spans are selected so that all mascons are approximately the same area, and a spherical cap mascon is used at each pole), but have now improved global signal recovery with the application of a new regularization strategy. The original solution was successful at its intended purpose to accurately recover high-latitude land ice changes, but the regularization matrices (equal to the inverse of the signal covariance) had not yet been globally optimized. The new product presented here improves global signal recovery by combining solution iteration with a new approach to spatiotemporally bin the inter-satellite range-acceleration residuals in the design of time-dependent regularization matrices. Our strategy is conservative by design in an effort to minimize the role of the regularization scheme on the final solution.

We also present a new detailed assessment of the solution uncertainties, which includes the data-driven estimation of the solution covariance (noise) and new estimates of solution bias (leakage) determined by monthly resolution operators. A simple procedure for end users to construct the total uncertainties of the GSFC mascon product for both individual mascons and regional analyses is provided, and the results are validated against and compared to several independent data sets.

We conclude by applying the new solution and uncertainties to determine the mass contributions to global mean sea level (GMSL), and demonstrate successful closure of the GMSL budget. The processing and estimation strategies presented here will also form the basis for the NASA GSFC global mascon solutions in support of the GRACE Follow-On mission (GRACE-FO), which launched in May 2018.

2 Data and methods

2.1 Level 1B processing strategy and iteration

The GRACE gravity recovery processing procedures require the K-band range-rate (KBRR) inter-satellite measurements, GPS-determined satellite positions (Level 1B navigation files), star camera attitude data, and onboard accelerometer measurements of the non-conservative forces. Processing the Level 1B data also requires the application of forward models, which are needed to remove the effects of certain geophysical processes on satellite dynamics and the TVG estimates. These include the static gravity field, solid Earth and ocean tides, solid Earth and ocean pole tides, and atmosphere and ocean de-aliasing (AOD). The AOD product aims to mitigate the aliasing of the high-frequency atmosphere and non-tidal oceanographic signals into the monthly gravity solutions. It is important to note that the AOD model applied here is ECMWF/MOG2D (Carrère and Lyard 2003), which differs from the GRACE project AOD1B RL05.

We apply two notable design choices in our Level 1B processing strategy: the inclusion of additional TVG information in our set of forward models, and solution iteration. Prior studies have demonstrated the benefit of forward modeling the TVG signals of known hydrologic processes toward the further reduction of the KBRR residuals and mitigation of signal leakage (Luthcke et al. 2008; Sabaka et al. 2010). This strategy, however, requires the output of a high-quality hydrologic model, which is not readily available in near real time, as would be needed to meet GRACE-FO solution latency requirements. Instead, we choose to apply GRACE-derived trend and annual TVG signals in our a priori set of forward models, which is also an effective approach to reduce the magnitude of the KBRR residuals and the corresponding adjustment to the mascon parameters. Specifically, we apply the best-fit trend and annual periodic regression of a previous mascon solution (GSFC v1.1) and extrapolate the values forward in time to cover the current data span. We plan to utilize the same approach for constructing the a priori TVG portion of the forward models for GRACE-FO processing. The starting model does not necessarily need to be computed from an earlier GSFC mascon solution, but could be determined from any TVG product appropriately placed onto the GSFC mascon grid. However, it is important to note that if the selected TVG forward model contains information outside the spatiotemporal spectrum of the monthly mascon adjustments, then that portion of the signal will pass through unaffected to the final solution (e.g., AOD or hydrologic model output smaller than ~ 300 km). The starting model applied here is within the observable spectrum of the monthly adjustments, so is not expected to affect the final solution, and is included to improve the determination of the arc-specific parameters (discussed below) and facilitate solution convergence. The inclusion of additional TVG information in the forward model is analogous to the selection of a reference model when estimating the static gravity field (e.g., Pavlis et al. 2012).

The benefit of an iterative solution strategy was demonstrated in Luthcke et al. (2013) by the increased signal-to-noise ratio with each iteration until the solution converged. The same general strategy is applied here and is summarized in Table 1. The initial processing of the Level 1B data applies the a priori TVG signal discussed above, and produces the first adjustment to the mascon parameters, $\Delta\hat{\mathbf{h}}_1$. The iterative mascon updates have dimension $M \times N$ and are defined by

$$\Delta\hat{\mathbf{h}}_{\text{iter}} \equiv [\hat{\mathbf{m}}_1, \hat{\mathbf{m}}_2, \dots, \hat{\mathbf{m}}_M]_{\text{iter}}^T, \quad (1)$$

where $\hat{\mathbf{m}}_i$ is the $N \times 1$ global mascon estimate for the i th month, M is the number of months, and N is the number of mascons (41,168). With each iterative mascon adjustment, the TVG forward model is updated, the Level 1B data are reprocessed, and a new set of monthly mascons is estimated.

Table 1 Overview of iterative processing and solution strategy

Iter.	TVG forward model	Output
1	Trend and annual	$\Delta \hat{\mathbf{h}}_1$
2	Trend and annual + $\Delta \hat{\mathbf{h}}_1$	$\Delta \hat{\mathbf{h}}_2$
3	Trend and annual + $\Delta \hat{\mathbf{h}}_1 + \Delta \hat{\mathbf{h}}_2$	$\Delta \hat{\mathbf{h}}_3$
4	Trend and annual + $\Delta \hat{\mathbf{h}}_1 + \Delta \hat{\mathbf{h}}_2 + \Delta \hat{\mathbf{h}}_3$	post-fits

Iteration continues until convergence occurs, with our analysis showing that three iterations are sufficient. The final $M \times N$ mascon solution matrix, $\hat{\mathbf{x}}$, is then defined as the sum of the a priori model (trend and annual) and the full set of iterative updates:

$$\hat{\mathbf{x}} \equiv \text{a priori model} + \sum_{\text{iter}=1}^3 \Delta \hat{\mathbf{h}}_{\text{iter}}. \tag{2}$$

We execute a fourth and final processing of the Level 1B data in order to generate the true post-fit inter-satellite residuals, which confirm solution convergence and aid in validating the estimated mascon uncertainties, as discussed in Sect. 2.4.1. The effect of iteration on the mascon solution and inter-satellite range-acceleration residuals is illustrated in Figs. 1 and 2. In Fig. 1, we show the mass change time series and corresponding range-acceleration residuals for individual mascons in three distinctly different regions: the West Antarctic Ice Sheet, Gulf of Alaska, and the Chesapeake drainage basin. It is interesting to note the different convergence behavior of the different mascons, specifically, the nonlinear convergence behavior of the residuals in West Antarctic Ice Sheet, and the more rapid convergence in Gulf of Alaska where a separate constraint region is defined. Figure 2 presents the global picture of convergence, with maps of the root mean square (RMS) of the range-acceleration residuals. The lack of coherent signal that remains in the final post-fits (iteration 4) confirms that the solution has converged. The daily time series of inter-satellite range-acceleration residuals used throughout are determined as in Loomis and Luthcke (2017), which applies a simple low-pass filter to the KBRR residuals followed by quadratic Lagrange polynomial numerical differentiation. This procedure suppresses the high-frequency component that is geophysically uncorrelated and dominated by the spacecraft instrument noise.

Each GRACE processing center has a unique set of arc-specific parameters that are applied to the determination of the satellite orbits and/or co-estimated with the gravity parameters (note that for the sake of simplicity, these parameters are not explicitly included in the equations developed below). For each iteration, we process the KBRR and navigation files in daily arcs, and converge the following set of arc parameters with the updated TVG model: daily 12-

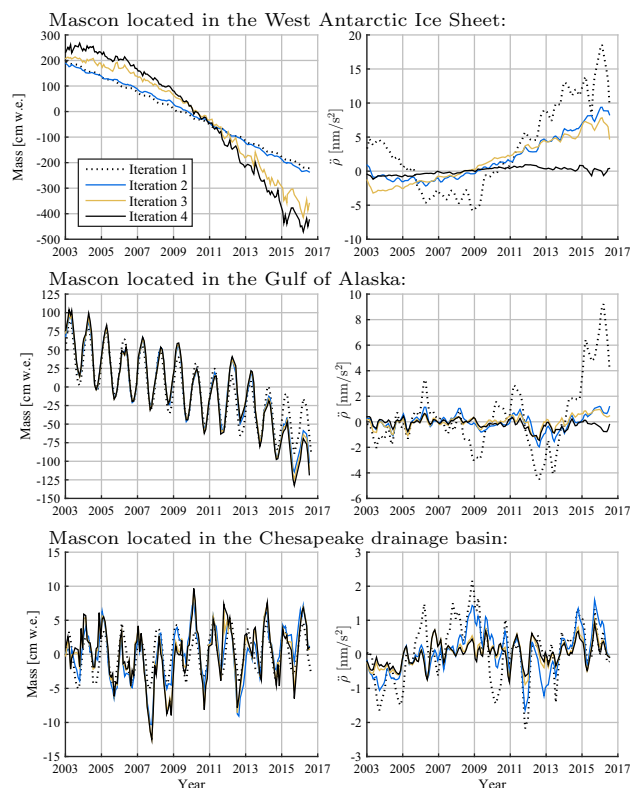


Fig. 1 Iterative solutions and residuals of sample individual mascons. (Left column) The effect of iteration on recovered mass change. (Right column) The effect of iteration on the binned range-acceleration residuals, $\hat{\rho}$. (Top row) Mascon located in the West Antarctic Ice Sheet, between Pine Island Glacier and Thwaites Glacier. (Middle row) Mascon located in the Gulf of Alaska. (Bottom row) Mascon containing Greenbelt, MD, USA, located in the Chesapeake drainage basin. The iteration numbers follow the definitions in Table 1, where iteration 4 defines the final mass change solution and the post-fit residuals to the final solution

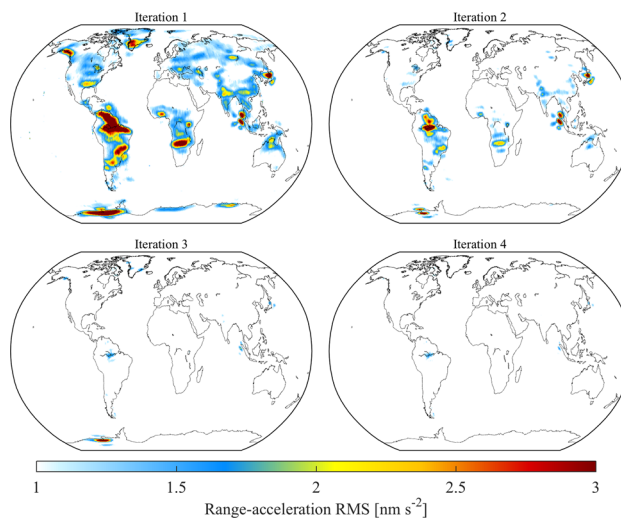


Fig. 2 RMS of the mascon-binned range-acceleration residuals for all four iterative Level 1B processing steps. See Table 1 and text in Sect. 2.1 for details

parameter satellite initial states, 3-hourly KBRR constant, trend, and one cycle-per-revolution measurement biases, 1.5-hourly 3-D accelerometer biases, and 1.5-hourly 3-D one cycle-per-revolution empirical accelerations. We then form monthly KBRR-only normal equations (including the regularization matrix discussed below) and solve for the following set of parameters: global mascons, the baseline parameter satellite initial states (Rowlands et al. 2002), and the KBRR measurement biases. The accuracy of the final mascon estimates may be affected somewhat by the selected set of non-gravitational state parameters and their errors, and quantifying this error type is beyond the scope of this study, and to our knowledge has not been analyzed for other GRACE data products. We expect that the iterative solution approach applied here minimizes the impact of the arc-specific parameters, as they are re-converged after each update to the TVG model.

Our choice to omit the actual GPS measurements in favor of the Level 1B navigations files significantly reduces the computer processing time, which is a major advantage when applying our iterative solution procedure. However, it is important to note that the satellite orbits contained in these files have been fit to a static gravity field, making them at a certain level incompatible with the KBRR measurements of TVG. This issue is easily addressed by first tuning our orbit and arc parameters with an existing TVG solution (a low degree expansion of Stokes coefficients is sufficient, e.g., 10×10) prior to initiating the iterative solution process summarized in Table 1. We have observed that failing to properly calibrate the orbits prevents the full recovery of some low degree Stokes coefficients, particularly the sectorals. The low degree portion of the gravity field is well determined by all of the readily available Level 2 products (except C_{20} which is replaced by the value determined from Satellite Laser Ranging) and is unaffected by the mascon regularization; therefore, the “value added” of mascon estimation is only relevant for Stokes degree and order above ~ 10 (Watkins et al. 2015).

2.2 Mascon regularization

2.2.1 Mathematical formulation

The regularized mascon system of equations for a particular month and iteration is described by:

$$\begin{aligned} \mathbf{d} &= \mathbf{A}\mathbf{m} + \nu, \nu \sim \mathcal{N}(0, \mathbf{W}^{-1}) \\ \mathbf{A} &\equiv \mathbf{H}\mathbf{L} \\ \mathbf{m}_a &= \mathbf{m} + \eta, \eta \sim \mathcal{N}(0, (1/\lambda)\mathbf{P}^{-1}), \end{aligned} \quad (3)$$

where \mathbf{m} is the global set of mascon parameters for one month, \mathbf{A} is the design matrix, \mathbf{H} contains the partial

derivatives of the KBRR measurements with respect to the differential Stokes coefficients, \mathbf{L} contains the partial derivatives of the differential Stokes coefficients with respect to the mascon parameters, \mathbf{d} is the KBRR measurement residuals, and \mathbf{m}_a is the a priori mascon state. The notation \mathcal{N} describes Gaussian distributed random errors with a certain mean and covariance so that ν describes the data noise with zero mean and covariance \mathbf{W}^{-1} , and η describes the a priori state uncertainty with zero mean and signal covariance $(1/\lambda)\mathbf{P}^{-1}$. The term λ is a scalar damping parameter that is tunable to provide the desired level of regularization. If we assume the a priori mascon state \mathbf{m}_a is zero, and seek to minimize the cost function:

$$J(\mathbf{m}) = \nu^T \mathbf{W} \nu + \eta^T \lambda \mathbf{P} \eta, \quad (4)$$

we arrive at the least-squares mascon estimate:

$$\hat{\mathbf{m}} = (\mathbf{A}^T \mathbf{W} \mathbf{A} + \lambda \mathbf{P})^{-1} \mathbf{A}^T \mathbf{W} \mathbf{d}, \quad (5)$$

which is commonly referred to as Tikhonov regularization (Tikhonov 1963), and can be described by the Wiener-Kolmogorov filter (Foster 1961).

The applied regularization, $\lambda \mathbf{P}$, is the most critical design consideration for producing mascon solutions, and a primary focus of this work is the newly developed strategies to define the monthly regularization matrices, \mathbf{P} . Departing somewhat from the solution presented in Luthcke et al. (2013), we have removed the temporal constraints and now only apply spatial regularization in the estimation of independent monthly solutions. Our \mathbf{P} is developed below, where Eqs. 6–11 are the same as Eqs. 18–23 in Sabaka et al. (2010) except for Eq. 8, which has been modified to include a new mascon-dependent weighting.

We begin by defining the $N(N-1)/2 \times N$ discrete first-difference operator constraint matrix \mathbf{D} , where the k th row constrains the i th and j th mascons:

$$D_{ki} = 1, \quad D_{kj} = -1, \quad D_{kq} = 0 \text{ for all } q \neq i, j. \quad (6)$$

The constraint equations are written as

$$\mathbf{0} = \mathbf{D}\mathbf{m} + \mathbf{e}, \quad (7)$$

where \mathbf{e} is assumed to be a Gaussian distributed error with zero mean and covariance $\mathbf{\Gamma}^{-1}$, denoted as $\mathbf{e} \sim \mathcal{N}(0, \mathbf{\Gamma}^{-1})$. The components of the diagonal matrix $\mathbf{\Gamma}$ are defined by

$$\Gamma_{kk} = \begin{cases} \exp\left(1 - \frac{d_{ij}}{D}\right) \frac{w_i + w_j}{2}, & \psi_i = \psi_j \\ 0, & \psi_i \neq \psi_j, \end{cases} \quad (8)$$

where D is the correlation distance, d_{ij} is the distance between mascon centers, w_i and w_j define the new mascon-dependent weighting, and ψ_i and ψ_j designate the constraint region for the i th and j th mascons. We enforce conservation of mass by appending Eq. 7 with an additional constraint as

$$\begin{pmatrix} \mathbf{0} \\ 0 \end{pmatrix} = \begin{pmatrix} \mathbf{D} \\ \mathbf{1}^T \end{pmatrix} \mathbf{m} + \begin{pmatrix} \mathbf{e} \\ e \end{pmatrix}, \tag{9}$$

where $\mathbf{1}$ is a vector of ones and $e \sim \mathcal{N}(0, w_c^{-1})$. As noted by Sabaka et al. (2010), this additional constraint is needed because the constant vector $\mathbf{1}$ is in the null spaces of \mathbf{L} and \mathbf{D} , meaning a uniform layer of mass over the sphere will not produce observable gravity signals in the KBRR measurements. The augmented system of equations in Eq. 9 is rewritten as

$$\mathbf{0} = \overline{\mathbf{D}}\mathbf{m} + \overline{\mathbf{e}}, \tag{10}$$

and our final \mathbf{P} is defined by

$$\mathbf{P} = \overline{\mathbf{D}}^T \overline{\mathbf{\Gamma}} \overline{\mathbf{D}}, \tag{11}$$

where the upper left portion of $\overline{\mathbf{\Gamma}}$ contains $\mathbf{\Gamma}$ and the lower right diagonal is w_c . Assigning a value of 10 to w_c is sufficient to ensure that the inversion in Eq. 5 exists and that mass is conserved.

2.2.2 Regularization regions

The constraint regions referenced in Eq. 8 have been slightly modified from those used in Luthcke et al. (2013). The new solution defines eleven constraint regions, for which mascons in separate regions are uncorrelated. These regions are Greenland Ice Sheet low elevation (< 2000 m), Greenland Ice Sheet high elevation (> 2000 m), Antarctic Ice Sheet including the Ronne and Ross ice shelves, Gulf of Alaska, land, ocean including smaller ice shelves, Mediterranean Sea, Black Sea, Red Sea, Caspian Sea, and Hudson Bay. The correlation distance, D , in Eq. 8 is 100 km everywhere except in the Antarctic Ice Sheet constraint region where the spatiotemporal sampling of the GRACE ground tracks supports a value of 50 km.

2.2.3 Iterative regularization design motivations

The most significant improvement in the regularization design is through the introduction of the mascon-dependent weighting in Eq. 8. The strategy for building these weights differs between the first iteration and subsequent iterations. The goal of the first iterative mascon adjustment, $\Delta\mathbf{h}_1$, is to recover the large spatial scale components of TVG not contained in the a priori model, so the initial regularization matrix is intentionally overconstrained. The GRACE error

analysis of Wahr et al. (2006) demonstrated a strong latitude dependence in the Stokes errors, presumably due to the spatiotemporal sampling, where midlatitude bands have higher errors than high-latitude bands due to fewer observations per degree longitude. We apply this known error structure in the design of a static (same for all months) set of mascon weights, and select the damping parameter, λ , so that the north–south striping patterns contained in unregularized GRACE solutions are not present in the mascons. Preserving the latitude dependence, we scale the ocean weights by a factor of 10 to account for the lower signal-to-noise ratio relative to the land and ice regions in the initial iteration.

A distinctly different regularization strategy is used for all subsequent iterations ($\Delta\mathbf{h}_2$ and $\Delta\mathbf{h}_3$), where the remaining Level 1B inter-satellite residuals are applied in the construction of Eq. 8 mascon weights. This new approach was largely motivated by the results of Loomis and Luthcke (2017), which demonstrated a strong linear relationship between unresolved local mass signals and the local range-acceleration residuals, once the long-wavelength components of TVG have been well determined. Similarly, justification for our regularization design strategy can be inferred from the discussion and analysis of the acceleration approach presented in Weigelt (2017). To briefly summarize, the derived range-acceleration gravimetric observable is written as

$$\ddot{\rho} = \ddot{\mathbf{x}}_{AB} \cdot \mathbf{e}_{AB} + \frac{1}{\rho} \dot{\mathbf{x}}_{AB} \cdot \dot{\mathbf{x}}_{AB} - \frac{\dot{\rho}^2}{\rho}, \tag{12}$$

where ρ , $\dot{\rho}$, and $\ddot{\rho}$, respectively, are the inter-satellite range, range-rate, and range-acceleration, $\dot{\mathbf{x}}_{AB}$ and $\ddot{\mathbf{x}}_{AB}$, respectively, are the velocity and acceleration difference vectors between the two GRACE satellites, and \mathbf{e}_{AB} is the line-of-sight direction unit vector between the satellites. The first term on the right-hand side of Eq. 12 is a direct function of the desired gravity parameters, while the remaining components of the right-hand side are termed the centrifugal acceleration. When working with residual quantities to a reference gravity field and reference orbit (e.g., $\delta\ddot{\rho} = \ddot{\rho} - \ddot{\rho}_{ref}$), the magnitude of the centrifugal component is sufficiently small at higher spatial frequencies (Stokes degree and order > 10) that it can be ignored. In other words, once the lower frequency signals in the gravity field have been well recovered, as is the case beginning with the second iteration, the remaining signals in the range-acceleration residuals are linearly related to unresolved TVG (i.e., $\delta\ddot{\rho} \approx \delta\ddot{\mathbf{x}}_{AB} \cdot \mathbf{e}_{AB}$), and that useful information is applied in creating unique regularization matrices for each iteration and month.

Procedurally, we bin the mission-long set of range-acceleration residuals by mascon, storing the mascon number, time tag, satellite altitude, and value of every residual for the duration of the mission. This binning procedure creates a time series with irregular temporal sampling for each

mascon, which is then Gaussian smoothed with $\sigma = 30$ days and resampled at the center of each GRACE monthly window. The applied smoothing procedure is effectively the same as computing monthly means within each mascon, but does allow some influence from data in neighboring months, which is helpful in obtaining reliable values for mascons with fewer observations. The global set of binned and smoothed range-acceleration values for a particular GRACE month defines the inverse ($1/w$) of the month-dependent mascon weights in Eq. 8. It is useful to note the conceptual difference here to iteratively reweighted least squares (IRLS), which assumes that larger residuals are indicative of less reliable data and so reduces their effect on the solution by decreasing the data weights defined by \mathbf{W} . In our case, we are instead assuming that larger residuals are not errors in the data, but rather due to unresolved TVG signal, so we decrease the weighting applied by \mathbf{P} for particular mascons to allow weak restrictions for those parameters.

The residual binning procedure is illustrated in Fig. 3, and shows the monthly map of binned residuals for a particular month along with the full time series of all binned residuals for a single mascon. The regularization damping parameter, λ , is empirically determined to be just large enough to suppress the non-geophysical north–south striping errors that primarily result from the lack of sensitivity of the inter-satellite measurements to the east–west gravity gradients. A similar empirical approach for selecting the damping parameter is also applied by Luthcke et al. (2013) and Watkins et al. (2015). The iterative estimation procedure applied here allows for a gradual reduction in the magnitude of the damping parameter through the final iterative adjustment.

We note one final important difference between the current mascon estimation procedure and the iterative Gauss–Newton nonlinear constrained least-squares procedure applied in Luthcke et al. (2013), which used the same regularization matrix with each iteration. As summarized in Table 1 and Eq. 5, we treat each re-processing of the Level 1B data as an independent regularized linear least-squares problem, where we update the starting model using the mascon update from the previous iteration, and reset the a priori state vector, \mathbf{m}_a , to be equal to zero. Recognizing the useful information available in the range-acceleration residuals for the redesign of regularization matrices for each iteration and month, we instead have adopted the approach presented here, which leverages valuable information to guide the solution path toward the final solution for which the residuals have been sufficiently minimized.

2.3 Mascon post-processing

There are several post-processing steps commonly applied to GRACE TVG solutions, whether in Stokes coefficients or

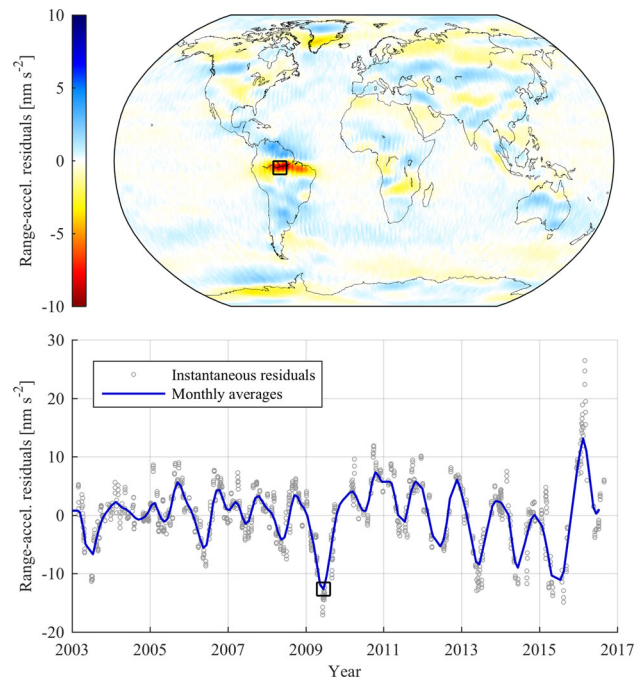


Fig. 3 Overview of iterative procedure to design monthly regularization matrices. (Top) Map of binned range-acceleration residuals for June 2009. (Bottom) Time series of binned range-acceleration residuals for a single mascon in the Amazon basin. This information is used to define the mascon-dependent weights in Eq. 8

mascon form. First, the GRACE satellites are insensitive to variations in the geocenter, so we apply a degree 1 correction to our mascon solution following the procedure in Swenson et al. (2008). Next, GRACE TVG solutions are known to provide poor estimates of C_{20} , so those are replaced with the values determined from Satellite Laser Ranging provided in GRACE Technical Note 07 (Cheng et al. 2013). We also follow the recommendations of Wahr et al. (2015) by adjusting the trends of C_{21}/S_{21} in order to remove the GIA trend component of the long-term changes to the pole tide. Note that this C_{21}/S_{21} correction will not be needed for future GSFC mascon solutions (after v02.4), as we will be adopting an updated linear mean pole model.

Designing mascon regularization matrices to maximize signal recovery while minimizing noise is a challenging problem, and we acknowledge that a very small subset of adjusted mascon parameters over the course of the mission could be unrealistic due to data noise or poor spatiotemporal sampling of particular mascons. Rather than over-regularizing the solution to address these outliers, we have instead chosen to perform a simple outlier detection-and-replacement procedure prior to releasing our solution that identifies all mascons over the course of the mission that are $5\text{-}\sigma$ outliers, and replaces them with values that are linearly interpolated from neighboring months. The number of identified outliers represents $\sim 0.002\%$ of the total set of mascon parameters.

Table 2 Summary of available GSFC mascon solutions available for download at <https://neptune.gsfc.nasa.gov/grace/>

Solution name	Description	Applications
v02.4	Comparable to GRACE Project GSM after corrections	Terrestrial water storage and cryosphere <i>after</i> removal of GIA
v02.4-ICE6G	v02.4 – GIA (Peltier et al. 2015)	Terrestrial water storage and cryosphere
v02.4-GeruoA	v02.4 – GIA (AG and Zhong 2013)	Terrestrial water storage and cryosphere
v02.4-GeruoA_OBP	v02.4 – GIA + AOD _Δ ^a + GAD ^b	Ocean bottom pressure, comparable to bottom pressure recorder data and other mascon solutions
v02.4-GeruoA_SLA	v02.4 – GIA + AOD _Δ ^a + GAD ^b – $\overline{\text{GAD}}^c$	Ocean mass, comparable to steric-corrected sea level anomalies

^a GSFC uses a different AOD model than the GRACE project GAD, so the model differences must first be restored

^bThe GAD contains the monthly surface pressure means of the non-tidal and atmospheric models used in Level 1B processing.

^cThe mean of GAD over the entire ocean is removed

Similarly, we also interpolate all of the Antarctic Ice Sheet values in July 2015 due to the lack of GRACE measurements in that region for that particular month.

Lastly, in order to facilitate the application of our mascon product to a variety of geophysical applications, we have elected to provide multiple versions of our mascons with various models removed or restored, as summarized in Table 2. Our current solution is v02.4, and the standard version is comparable in information content to the GRACE Project Level 2 Stokes solutions with the geocenter, C_{20} , and C_{21}/S_{21} post-processing corrections applied. Additionally, we provide two separate solutions where the GIA models, Peltier et al. (2015) and AG and Zhong (2013), have been removed. Finally, we provide two different ocean-only solutions, OBP and SLA, both of which have removed the AG and Zhong (2013) GIA model. The OBP solution is computed by restoring the surface pressure values of the atmospheric and non-tidal ocean model used in processing the Level 1B data (GAD), and is comparable to ocean bottom pressure recorder data and the ocean mascons provided by the Jet Propulsion Laboratory (JPL) and the University of Texas, Center for Space Research (CSR). The SLA solution removes the mean atmospheric surface pressure over the ocean from the OBP product, providing the ocean mass change variability, which can be compared to steric-corrected sea level anomalies observed by altimetry. As previously mentioned, current GSFC processing applies a different AOD model than that provided by the GRACE project, and this difference is accounted for in Table 2 with the term AOD_Δ, equal to the difference between ECMWF/MOG2D and the GRACE project AOD RL05 (ECMWF/OMCT).

2.4 Mascon error assessment

As defined in Eq. 3, we assume stochastic errors that are second-order stationary, which are fully described by their mean and covariance. The mean (bias) component to the error is often ignored, but we show in “Appendix A” that depending

on the assumed statistics, a regularized solution will indeed be biased, and that this component of the error must be considered in order to appropriately quantify the uncertainty of the estimated mascons. This conclusion is not limited to the GSFC mascons, but is arguably true for most regularized geophysical inversion problems, where the assumed statistics of the a priori state are likely invalid to some extent. These invalid assumptions are necessary to create an invertible system that provides solutions with any geophysical meaning, but it is important to consider their effect when defining the total uncertainty. First, we present the estimated covariance of the GSFC mascons, which is commonly the only component of the error that is considered. We then discuss the bias component, which in the context of GRACE gravity analysis is synonymous with the term “leakage,” and so the terms bias and leakage are used interchangeably throughout.

2.4.1 Mascon covariance

Following Eqs. 5 and A.12, the formal covariance for the mascon adjustment, $\hat{\mathbf{m}}_{ij}$, for the i th month and j th iteration, is defined by

$$\text{cov}(\hat{\mathbf{m}}_{ij}) = \left(\mathbf{A}_{ij}^T \mathbf{W} \mathbf{A}_{ij} + \lambda \mathbf{P}_{ij} \right)^{-1}. \tag{13}$$

Though readily available as a part of our processing, there are two issues with using this quantity for assigning noise uncertainties to the final mascon product. The first is that formal covariances usually need to be calibrated, and this is often done by scaling the covariance so that the variances approximately match the misfit to in situ data. The effectiveness of the calibration is then somewhat dependent on the assumed accuracy of the in situ data. This calibration process is a form of variance component estimation (VCE), details of which can be seen in Kusche (2003) with application to gravity estimation in Lemoine et al. (2013). The more significant issue in this context is the fact that the covariance in

Eq. 13 is for a particular iteration, and as we have discussed above, the regularization matrices, \mathbf{P}_{ij} , are updated with the range-acceleration pre-fit residuals on each iteration. In other words, for the regularization strategy adopted here, the result of Eq. 13 is only valid (though still uncalibrated) for a particular iteration.

To overcome this limitation, we have instead applied a data-driven approach to estimate the variance–covariance of the mascon parameters. We begin by defining the $M \times N$ noise matrix, $\hat{\mathbf{n}}$, as the difference between the solution and the temporally filtered mascon solution:

$$\hat{\mathbf{n}} \equiv \hat{\mathbf{x}} - \mathcal{F}(\hat{\mathbf{x}}), \tag{14}$$

where $\mathcal{F}(\cdot)$ is a second-order Savitzky–Golay filter (Savitzky and Golay 1964), which has been selected so that it approximately matches the noise level predicted by the post-fit observation residuals (discussed below). If we assume that $\mathbb{E}[\hat{\mathbf{n}}]=0$, then the spatial error covariance, \mathbf{C}_s (dimension $N \times N$), and temporal error covariance, \mathbf{C}_t (dimension $M \times M$), are, respectively, defined and computed as,

$$\begin{aligned} \mathbf{C}_s &= \mathbf{C}_{(\hat{\mathbf{x}}-\mathbf{x})_s} = \mathbf{C}_{(\hat{\mathbf{n}})_s} \\ &= \mathbb{E} \left[(\hat{\mathbf{n}} - \mathbb{E}[\hat{\mathbf{n}}]) (\hat{\mathbf{n}} - \mathbb{E}[\hat{\mathbf{n}}])^T \right] \\ &= \frac{1}{N-1} \sum_{i=1}^N \hat{\mathbf{n}} \hat{\mathbf{n}}^T \\ \mathbf{C}_t &= \mathbf{C}_{(\hat{\mathbf{x}}-\mathbf{x})_t} = \mathbf{C}_{(\hat{\mathbf{n}})_t} \\ &= \mathbb{E} \left[(\hat{\mathbf{n}}^T - \mathbb{E}[\hat{\mathbf{n}}^T]) (\hat{\mathbf{n}}^T - \mathbb{E}[\hat{\mathbf{n}}^T])^T \right] \\ &= \frac{1}{M-1} \sum_{i=1}^M \hat{\mathbf{n}}^T \hat{\mathbf{n}}. \end{aligned} \tag{15}$$

The square root of the diagonal elements of \mathbf{C}_s and \mathbf{C}_t defines the noise standard deviation map and time scales shown in Fig. 4, respectively. If we define the time scale of the i th month as $T(i) \equiv \sqrt{\mathbf{C}_t(i, i)}$, then the i th month and the k th mascon components of the $M \times N$ noise standard deviation matrix are defined as

$$\hat{\sigma}_{ik} = T(i) \sqrt{\mathbf{C}_s(k, k)}. \tag{16}$$

The covariance matrices in Eq. 15 and the final noise estimate in Eq. 16 are only valid if the selected temporal filter, \mathcal{F} , produces an estimated noise matrix, $\hat{\mathbf{n}}$, that well describes the true noise of the solution, $\hat{\mathbf{x}}$. (The noise could be under- or overestimated based on the aggressiveness of the filter.) To validate the selected temporal filter, we compare the gravity degree variance of the spatial standard deviation (temporal mean of Eq. 16) to that predicted by the KBRR post-fit residuals as determined by the semi-analytic error

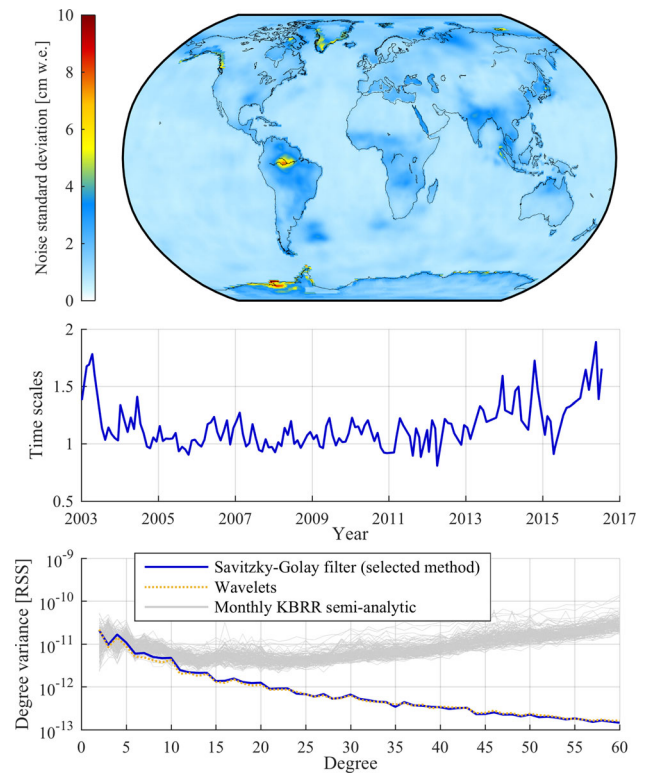


Fig. 4 Noise covariance results and validation. (Top) Global map of noise standard deviation values; equal to the square root of the diagonal elements of the spatial covariance in Eq. 15. (Middle) Time series of temporal standard deviation, or time scales that should be applied to the spatial map; equal to the square root of the diagonal elements of the temporal covariance in Eq. 15. (Bottom) Validation of the selected Savitzky–Golay filter used to define the covariance matrices; results are compared to a wavelet-based noise assessment, and a semi-analytic approach that uses the KBRR post-fit residuals

analysis procedure described in Sect. 3.7.1 of Kim (2000). It is well known that the degree variance of the GRACE-derived Stokes coefficient errors increases dramatically at higher degrees, while the degree variance of the TVG signal we seek to recover decreases. The benefit of regularized TVG estimation is demonstrated in the spectral domain by the fact that the degree variance of the recovered TVG approximates the expected TVG signal (see (Rowlands et al. 2010) for a detailed discussion). This divergent behavior between the gravity degree variances of regularized and unregularized estimates of TVG is true of both the signals and the errors, a fact that is relevant to the efforts to validate our mascon uncertainties, as the regularized and unregularized error assessments will diverge above the lowest Stokes degrees where the effects of regularization are clearly seen.

To that end, Fig. 4 compares the monthly degree error variances determined from the KBRR residuals (Kim 2000) to that determined by the selected Savitzky–Golay filter, where the former is descriptive of the unregularized TVG solution. This comparison is then only expected to be valid at the low-

est degrees, which is exactly what is observed in Fig. 4. The ratio of the average KBRR-determined errors and the Savitzky–Golay errors is between 0.5 and 2.0 for all Stokes degrees 10 and below, that is, the ratios are close to 1.0 and the actual noise-related errors are well described by the selected filter.

As an additional validation exercise, we also apply wavelets in the computation of the spatial noise standard deviation map following the method discussed in Donoho and Johnstone (1994) and Loomis and Luthcke (2014). This wavelet-based validation is useful because there are no parameters that need to be tuned, unlike the Savitzky–Golay filter. Figure 4 shows excellent agreement between the selected Savitzky–Golay filter and the independent wavelet-based noise estimate.

2.4.2 Mascon bias (leakage)

The unregularized least-squares estimator (i.e., $\lambda=0$) is applied when solving for the GRACE Level 2 Stokes coefficients, in which case the estimate is guaranteed to be unbiased and the covariance matrix fully describes the uncertainty. Following the results of Eq. A.9, Hoerl and Kennard (1970), and Kusche and Springer (2017), the regularized mascon solution bias is equal to:

$$\mathbb{E} [\hat{\mathbf{x}} - \mathbf{x}] = (\mathbf{R} - \mathbf{I}) \mathbf{x}, \tag{17}$$

where \mathbf{x} is the unknown truth state, $\hat{\mathbf{x}}$ is the estimated state, and \mathbf{R} is the resolution operator:

$$\mathbf{R} \equiv (\mathbf{A}^T \mathbf{W} \mathbf{A} + \mathbf{P})^{-1} \mathbf{A}^T \mathbf{W} \mathbf{A}, \tag{18}$$

which may be used to relate the unknown truth state to the estimated state if noise is neglected (Menke 2015):

$$\hat{\mathbf{x}} = \mathbf{R} \mathbf{x}. \tag{19}$$

To test the validity of these expressions and their applicability to defining mascon uncertainty, we performed a simple one-month simulation. We generated a month of “truth” Level 1B KBRR observations for a certain set of background models, which are perfect noise-free observations of the “true” TVG field. If these perfect data are processed with the same exact set of background models, the observations agree perfectly with the model, and all mascon updates are equal to zero. We then perturbed the background model by a known amount \mathbf{x} , reprocess the data, and generate the mascon estimate, $\hat{\mathbf{x}}$. In this case, our perfect noise-free data will recover the perturbed field \mathbf{x} , up to the spatial resolution that is observable by GRACE. (We define the perturbed model as 10% of a single epoch of a high-resolution hydrology model averaged into the 1-arc-degree GSFC mascon grid, which

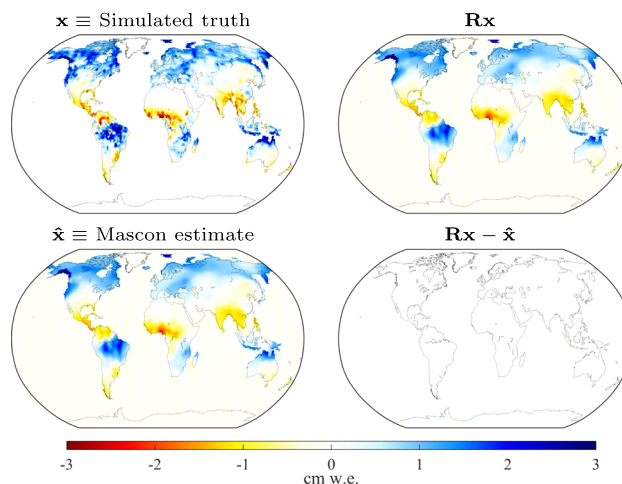


Fig. 5 Leakage simulation results. (Top left) Simulated high-resolution truth; $\text{RMS}_{\text{land}} = 0.90$ cm. (Top right) The resolution operator, \mathbf{R} , multiplied by the simulated high-resolution truth, \mathbf{x} ; $\text{RMS}_{\text{land}} = 0.72$ cm. (Bottom left) The estimated mascons, $\hat{\mathbf{x}}$, using the same regularization matrix, \mathbf{P} , used in the construction of the resolution operator, \mathbf{R} ; $\text{RMS}_{\text{land}} = 0.72$ cm. (Bottom right) The difference between the top right and bottom left; $\text{RMS}_{\text{land}} = 0.02$ cm. The excellent agreement between $\mathbf{R} \mathbf{x}$ and $\hat{\mathbf{x}}$ validates Eq. 19, and therefore the use of Eq. 17 for defining the leakage error

is a much higher than the true spatial resolution of monthly GRACE solutions. The model power was reduced to 10% to ensure that the large majority of recoverable signal would be obtained with a single iteration.) Finally, we apply the same processes and regularization matrix used to estimate the final (third) global mascon update for January 2006, in order to validate Eq. 19, i.e., that $\hat{\mathbf{x}} \approx \mathbf{R} \mathbf{x}$. The results of this simulation study are shown in Fig. 5, confirming the validity of using Eq. 17 to define the bias (leakage) of the mascon solutions.

Unlike for our simulated case, the true state in reality is unknown. We instead define for the i th month, the estimated bias, $\hat{\ell}_i$, by substituting the true monthly state with the estimated monthly state, $\hat{\mathbf{x}}_i$:

$$\hat{\ell}_i = (\mathbf{R}_i - \mathbf{I}) \hat{\mathbf{x}}_i. \tag{20}$$

The $N \times N$ resolution operator, \mathbf{R}_i , needs to be computed monthly as the \mathbf{A} and \mathbf{P} matrices in Eq. 18 are unique to each month. The same strategy to substitute the estimated state for the true state is mentioned by Kusche and Springer (2017) and was applied by Luthcke et al. (2013) for estimating regional leakage for land ice mass signals.

Upon inspection, the full set of leakage estimates, $\hat{\ell}$, contains both a deterministic (trend) and stochastic (other) component, so may be written as:

$$\hat{\ell} = \hat{\ell}_{\text{trend}} + \hat{\ell}_{\text{other}}, \tag{21}$$

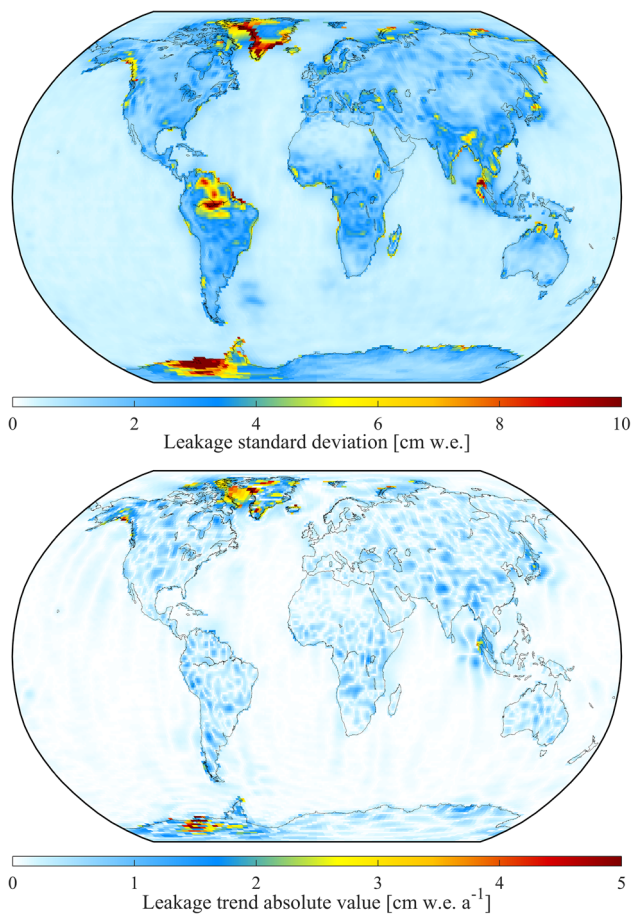


Fig. 6 Mascon leakage components. (Top) The standard deviation of the stochastic component of mascon leakage, $\hat{\ell}_{\text{other}}$. (Bottom) The trend component of mascon leakage, $\hat{\ell}_{\text{trend}}$. See Eq. 21

where $\hat{\ell}_{\text{trend}}$ contains the best-fit trends of $\hat{\ell}$, and $\hat{\ell}_{\text{other}}$ is what remains after removing $\hat{\ell}_{\text{trend}}$ from $\hat{\ell}$. In light of the assumption in Eq. 20 that $\mathbf{R}\mathbf{x} \approx \mathbf{R}\hat{\mathbf{x}}$, we do not directly apply the stochastic component of the leakage, $\hat{\ell}_{\text{other}}$, for constructing the total error budget. We instead assume that the distribution of $\hat{\ell}_{\text{other}}$ is a more accurate descriptor of the true bias than the individual values of $\hat{\ell}_{\text{other}}$, so define the stochastic portion of the leakage for the i^{th} month and the k^{th} mascon as

$$(\hat{\ell}_{\sigma})_{ik} = \sqrt{\frac{\sum_{j=1}^M (\hat{\ell}_{\text{other}}(j, k) - \frac{1}{M} \sum_{j=1}^M \hat{\ell}_{\text{other}}(j, k))^2}{M-1}}; \quad (22)$$

i.e., we compute the standard deviation over time for each mascon, noting that the estimated stochastic leakage error for each mascon defined in Eq. 22 is the same for all months. To summarize, the total leakage estimate for a single mascon is defined by two parameters: the leakage trend and the leakage standard deviation, which are applied in the $M \times N$

matrices $\hat{\ell}_{\text{trend}}$ and $\hat{\ell}_{\sigma}$, respectively. Maps summarizing the two components of leakage error are shown in Fig. 6.

It is important to note that the resolution operator, \mathbf{R} , as it is defined and applied here, is only valid for the case of a single iteration of linear least squares. As previously noted, we have modified the Gauss–Newton constrained nonlinear least squares of Luthcke et al. (2013) in favor of an iterative linear least-squares approach, in order to leverage the useful information contained in the range-acceleration residuals for the construction of month- and iteration-dependent regularization matrices. The final iteration is the least regularized, so the resolution operators from the final iteration are most descriptive of the resolution properties of the final mascon solution, $\hat{\mathbf{x}}$. This differs from the earlier discussion regarding the covariances, for which the iteration-dependent formal covariances were only valid for a particular mascon update, $\Delta \hat{\mathbf{h}}_{\text{iter}}$.

2.4.3 Building the total error budget

As detailed in Eqs. A.3 and A.4, the total error is defined by the sum of the error covariance and bias. We provide here a simple procedure to construct 1-dimensional Gaussian 95% uncertainties, for both individual mascons and regional analysis. To ensure that the provided uncertainties are at the level of $\sim 95\%$, we examine the statistics of $\hat{\mathbf{n}}$ and $\hat{\ell}_{\text{other}}$. Figure 7 compares the cumulative sum statistics for the noise $\hat{\mathbf{n}}$, the stochastic leakage $\hat{\ell}_{\text{other}}$, and a normal distribution. We observe that all curves include $\sim 95\%$ of data points at 2σ , even though the data distributions themselves deviate somewhat from the normal.

We conclude, then, that the $M \times N$ total 95% uncertainty for the mission-long set of individual mascons is defined by:

$$\varepsilon_{\text{mascon}} = |\hat{\ell}_{\text{trend}}| + 2(\hat{\ell}_{\sigma} + \hat{\sigma}), \quad (23)$$

and the uncertainty time series for the k^{th} mascon is the k^{th} column of $\varepsilon_{\text{mascon}}$. The three components that define Eq. 23 are provided separately with the GSFC mascon product. As previously noted, the values of $\hat{\ell}_{\sigma}$ are the same for all months. The leakage trend time series, $\hat{\ell}_{\text{trend}}$, is populated using an epoch of 2010.0, where the value is zero. The user can easily modify this epoch if desired.

As expected, the ratio of the signal to the uncertainty is quite low for most individual mascons. Regardless of methodology, GRACE is not able to fully resolve mass change at the 1-arc-degree spatial resolution that the GSFC mascons are estimated, and a more typical application of GRACE products is to aggregate the signal over a region of interest to determine the regional mass change time series. As the size of the region increases, the total noise and leakage errors are expected to decrease. In the case of uncorrelated

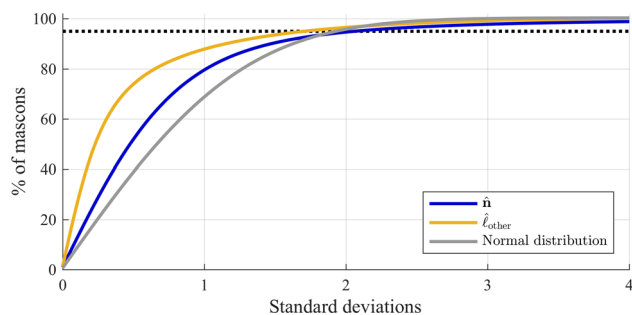


Fig. 7 Error distributions. The distribution of estimated errors is shown in terms of cumulative sum per standard deviation, for the estimated mascon noise, \hat{n} , the stochastic leakage component, $\hat{\ell}_{\text{other}}$, and a normal distribution. We note that all three contain $\sim 95\%$ of the data points at 2σ

errors, the standard error of the mean dictates that the factor $1/\sqrt{n}$ be applied, where n is the number of observations. We know, however, that the mascons within a region are highly correlated over a certain distance (i.e., the spatial resolution of the solution), so each mascon cannot be treated as an independent observation when defining the regional uncertainties. Accounting for the correlation between neighboring mascons, the regional 95% uncertainty time series is then defined as:

$$\varepsilon_{\text{region}} = |\hat{\ell}_{\text{trend}}| + \frac{2(\bar{\ell}_{\sigma} + \bar{\sigma})}{\sqrt{(n_{\text{region}}/z)}}, \tag{24}$$

where n_{region} is the number of mascons that defines the region, z is the number of mascons that defines the spatial resolution, and $\bar{\chi}$ indicates the average value of parameter χ in centimeters water height equivalent (abbreviated as cm w.e.), or equivalently the sum of the total mass in Gt. Appropriate values for z are easily determined using the set of resolution operators, by applying and analyzing the impulse response for mascons in various regions, and characterizing the spatial resolution at which distinct signals are observable. In other words, we compute $\hat{\mathbf{x}} = \mathbf{R}\mathbf{x}$, where \mathbf{x} has only one nonzero value, and we examine $\hat{\mathbf{x}}$ to define the resolution; this is similar to the approach discussed by Luthcke et al. (2013). We conclude that appropriate values are $z=6$ (resolution ~ 270 km) for regional analysis of the Antarctic Ice Sheet, and $z=22$ (~ 520 km) for regional analysis everywhere else. The reported resolutions are consistent with previously published results (Wahr et al. 2006; Luthcke et al. 2013), and the higher resolution at high latitudes agrees with the error analysis of Wahr et al. (2006). If $z \geq n_{\text{region}}$, we set $z = n_{\text{region}}$, as this indicates that all errors within the region are correlated. As an example, the components and total error budget for two different regions in the Antarctic Ice Sheet are shown in Fig. 8. The first shows the results for a smaller region with 20 mascons: basin 21 in Luthcke et al. (2013) which contains

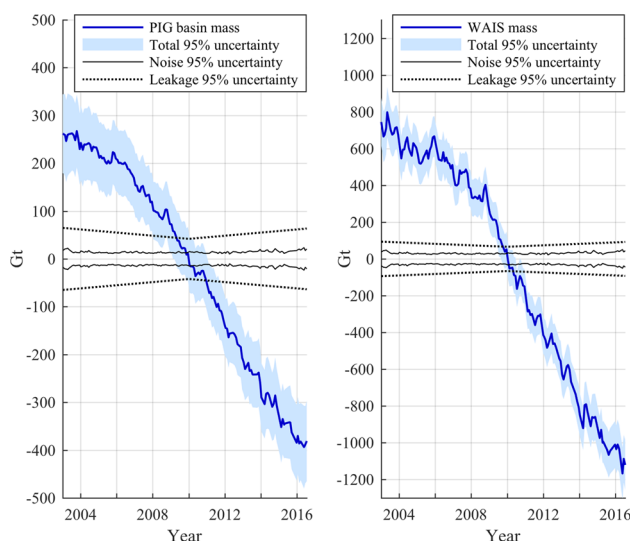


Fig. 8 Regional time series with uncertainties. (Left) Solution and uncertainties for Antarctic Ice Sheet basin 21, which contains Pine Island Glacier. (Right) Solution and uncertainties for West Antarctic Ice Sheet. These solutions have had the IJ05_R2 GIA model removed

the Pine Island Glacier (PIG). The second result is for the full West Antarctic Ice Sheet, which is defined by 223 mascons.

We note that the regional uncertainty time series defined by Eq. 24 uses the same three components as Eq. 23 ($\hat{\ell}_{\text{trend}}$, $\hat{\ell}_{\sigma}$, and $\hat{\sigma}$), which are provided with the GSFC mascon product. Alternatively, one could first compute the leakage time series as the average leakage over the basin: $\hat{y} = \bar{\ell}$, separate it into its deterministic and stochastic components: $\hat{y} = \hat{y}_{\text{trend}} + \hat{y}_{\text{other}}$, and then define the regional 95% uncertainty time series as:

$$\varepsilon_{\text{region}} = |\hat{y}_{\text{trend}}| + 2 \left(\hat{y}_{\sigma} + \bar{\sigma} / \sqrt{(n_{\text{region}}/z)} \right), \tag{25}$$

where \hat{y}_{σ} is the standard deviation of \hat{y}_{other} . This approach fully accounts for the shape of the selected basin, but numerous tests show little difference between the results of Eq. 24 and Eq. 25. All presented results apply Eq. 24, as we have elected not to distribute $\hat{\ell}$ with the mascon product in an effort to simplify the procedure for data users.

2.4.4 Uncertainty validation and comparison

We conclude this discussion on the total GSFC mascon uncertainties with comparative analysis to GRACE products released by other processing centers. First, we propose that if our total uncertainties are well defined, they should contain $\sim 95\%$ of independent mascon estimates, such as those provided by JPL and CSR. To that end, Table 3 summarizes the percentage of JPL and CSR mascon observations of mass change that are contained by the GSFC mascons and uncertainties for three separate cases: all 41,168 GSFC individual

Table 3 Comparison between GSFC mascon solution and uncertainties, to JPL and CSR mascon solutions. The provided values are the number of mission-long values contained within the 95% GSFC mascon uncertainties for both individual and regional analyses

Region	JPL mascons (%)	CSR mascons (%)
Individual mascons	92.8	95.6
Global hydrology basins	94.8	96.5
Antarctic Ice Sheet basins	95.2	94.8

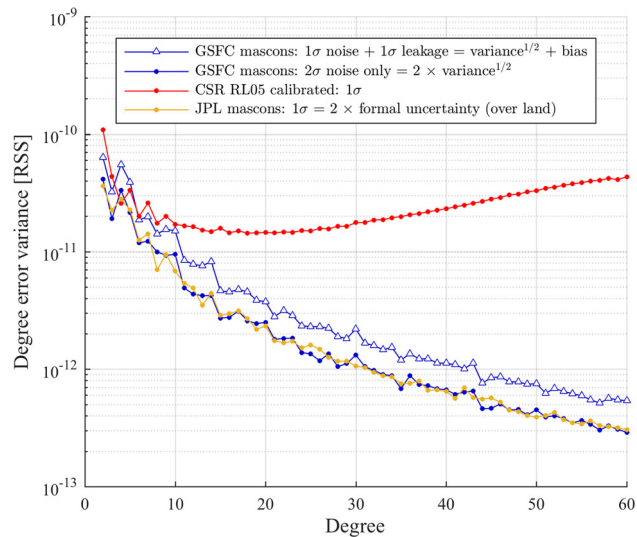


Fig. 9 GSFC mascon uncertainties. The estimated uncertainties for different components of the GSFC mascons are compared to the calibrated CSR RL05 Stokes coefficient uncertainties and the JPL RL2 mascon uncertainties. Refer to the text in Sect. 2.4.4 for detailed discussion

mascons (Eq. 23); the 187 largest global hydrology basins (Eq. 24 with $z=22$); and 36 drainage basins in the Antarctic Ice Sheet (Eq. 24 with $z=6$). The resulting percentages for all cases are remarkably close to the predicted value of 95%, providing strong evidence that our uncertainties are well defined.

Lastly, in Fig. 9 we compare the degree error variance of our uncertainties to the calibrated uncertainties provided for the CSR RL05 Stokes coefficients and the JPL RL2 mascons. We first note the excellent agreement between the 2σ GSFC noise-only (variance) uncertainties and the 1σ JPL uncertainties. As discussed in Wiese et al. (2016), the JPL mascon formal uncertainties have been scaled by a factor of 2 over land, where land signals dominate the power in both the solution and uncertainties. This result suggests that the JPL 1σ formal uncertainties approximately match the GSFC mascon noise-only uncertainties, and that the discrepancy between JPL and the GSFC total uncertainties is likely due to the fact that the bias/leakage component is not included in the estimated values for JPL. This result should not be interpreted as the GSFC product having larger errors in reality (when

aggregated to the same spatial scale as the JPL 3-arc-degree mascons). We also note that the total 1σ GSFC uncertainties show much better agreement with the calibrated 1σ CSR RL05 Stokes coefficient uncertainties at the low degrees than the JPL mascon uncertainties. As previously discussed, the Stokes uncertainties should only approximate the mascon uncertainties at the lowest degrees and will not have a bias component, as the Stokes coefficients are not regularized and are therefore unbiased.

3 Science results

The primary focus of this work has been to summarize the procedures applied in the estimation of GSFC mascons and the assessment of uncertainties. We conclude here with a brief summary of science results extracted from the latest product, highlighting the application of the new uncertainties.

Global maps of the best-fit mascon trend and annual amplitude are shown in Fig. 10. The first column of figures shows the global set of best-fit parameters, while the second shows the same values over land and ice, where we have highlighted the individual mascons with statistically significant fits. It is important to reiterate that this analysis is strictly related to the statistical significance of individual mascon fit parameters and is not at all indicative of the statistical significance of any regional analyses. The fit parameter 95% uncertainties are defined as the root sum squared (RSS) of the calibrated fit uncertainty, the stochastic noise and leakage, and the leakage trend. The calibrated trend fit is determined following Eq. 3.10 of Lee and Lund (2004), while the other components are defined in Eq. 23. The effect of the stochastic part is determined by applying a simple Monte Carlo approach where many random realizations of the time series are generated with the appropriate standard deviation and the resulting spread of the fit parameters is computed. The leakage trend component does not affect the annual amplitudes. Many maps similar to Fig. 10 have been produced from GRACE data, but this is the first that we are aware of that identifies individual locations where these important geophysical parameters are identified by their statistical significance. It is a notable achievement of the GRACE mission and the GSFC product that such a high percentage of fit parameters are statistically significant at 1-arc-degree spatial resolution. We have excluded the ocean here, as it is commonly analyzed in terms of ocean bottom pressure, which is the sum of the AOD surface pressure and the estimated mascons.

Many of the geophysical signals highlighted in Fig. 10 have been discussed at length in the scientific literature. The observed trends are significant for 59% of land and ice sheet mascons, where the largest negative trends are due to ice mass losses in the Greenland Ice Sheet and West Antarctic Ice Sheets, with other significant ice mass losses occurring in

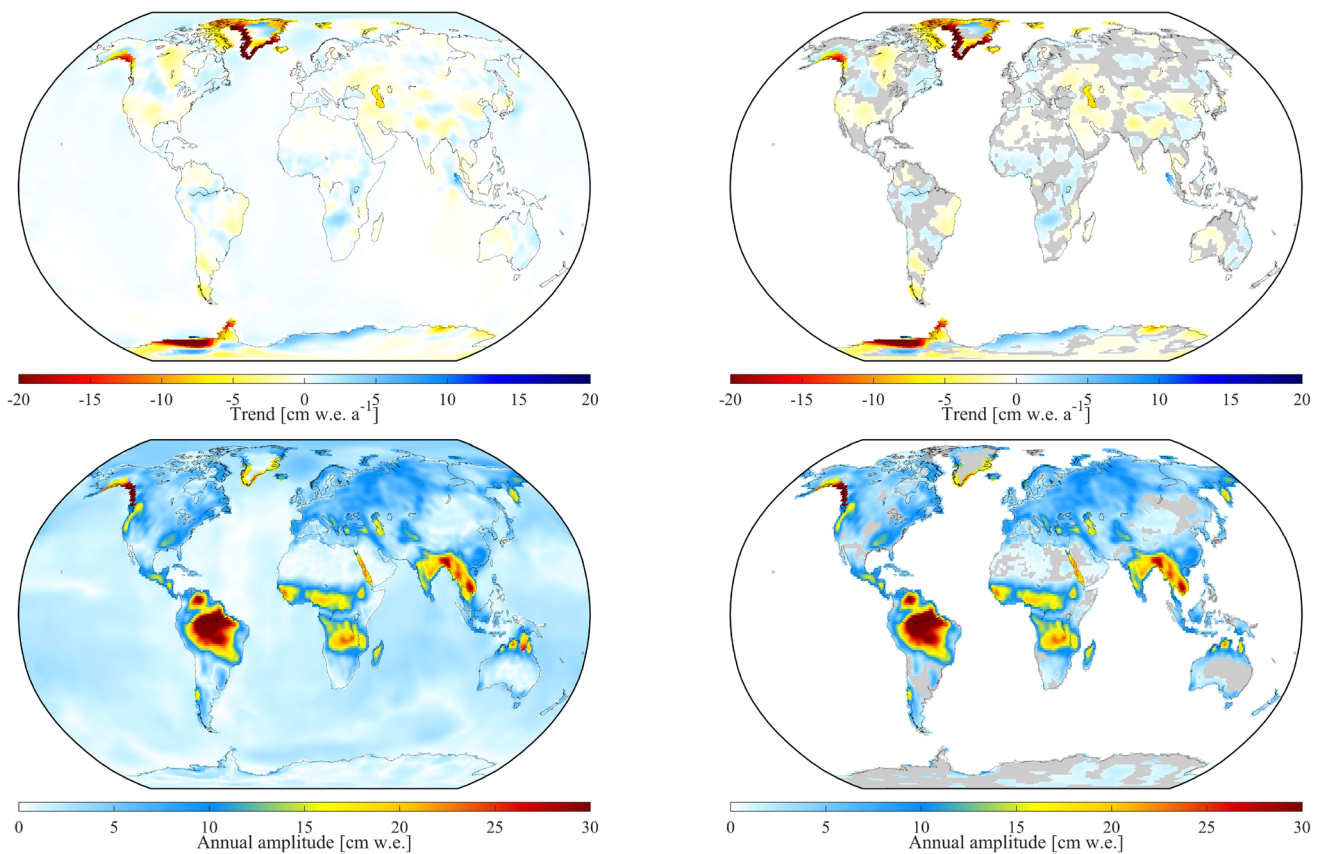


Fig. 10 Regression trend and annual amplitude best-fit parameters. (Top row) Global mascon trends. (Bottom row) Global mascon annual amplitudes. (Left column) All mascons. (Right column) Statistically significant land and ice sheet values are identical to values in the left

column, while lack of statistical significance is indicated by gray colored mascons. Important note: This analysis is strictly related to the statistical significance of individual mascon fit parameters and is not indicative of the statistical significance of regional analyses

the Antarctic Ice Sheet Peninsula, the Gulf of Alaska glaciers, the ice caps in and around the Ellesmere and Baffin Islands, and the Patagonia ice fields. Positive trends are observed in the northern interior of the Greenland Ice Sheet and in the Queen Maud Land region of the Antarctic Ice Sheet. Other notable trends are the result of changes in terrestrial water storage, with our results showing good qualitative agreement to other recent global hydrologic trend analyses (Reager et al. 2016; Scanlon et al. 2018; Rodell et al. 2018). Negative trends in terrestrial water storage are the result of climate variability, irrigation, and groundwater withdrawals, while positive trends are generally attributed to climate variability (Scanlon et al. 2018). The annual amplitudes are significant for 81% of mascons, where the lack of statistical significance exists primarily in arid regions, the interior of the Greenland Ice Sheet, and over large portions of the Antarctic Ice Sheet.

One of the most important applications of GRACE data has been the monitoring of the mass component of global mean sea level (GMSL). Total GMSL has been continuously observed by a series of satellite altimeter missions from the launch of TOPEX/Poseidon in 1992 up to the present day.

GMSL is the sum of the changes in ocean mass observed by GRACE, and the steric (density) changes. The steric component is primarily observed by in situ point measurements from the network of Argo floats that provide profiles of temperature and salinity, up to a depth of 2000 m. The Argo sampling has continuously improved, and began to produce reliable estimates of the steric contribution to GMSL around 2005 (Leuliette and Willis 2011). With concurrent observations of the total, mass, and steric components, it is possible to determine whether or not the GMSL budget is closed. Lack of budget closure could be the result of errors in one or more of the observation methods, or unobserved steric changes in the deep ocean.

In Fig. 11 and Table 4, we present the successful closure of the GMSL budget using the ocean mass change solution from the GSFC mascons, and the total GMSL and steric solutions presented in a recent survey of the global sea level budget (WCRP 2018). Over the common data span of 2005.0–2016.0, the sum of the full-depth steric and GSFC ocean mass trends is equal to $3.69 \pm 0.44 \text{ mm a}^{-1}$, achieving remarkable agreement with the total GMSL trend of

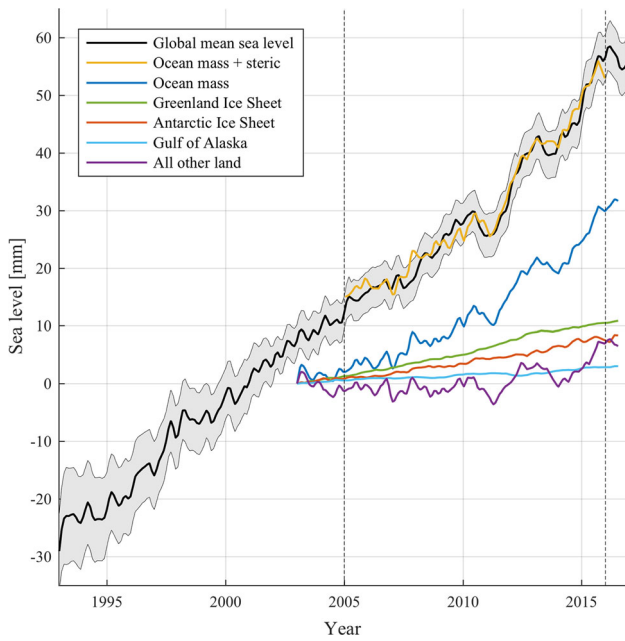


Fig. 11 Global mean sea level budget closure. GMSL (black) is the total change observed by multiple decades of sea surface altimetry measurements, along with 90% confidence interval (gray). The sum of the GSFC mascon total ocean mass and steric components (yellow) shows excellent agreement to the altimetry observations. The contributions to total ocean mass (dark blue) are shown for the Greenland Ice Sheet (green), the Antarctic Ice Sheet (orange), Gulf of Alaska (light blue), and all other land (purple). All time series have had the annual and semiannual components removed and Gaussian smoothing applied with $\sigma = 30$ days

$3.70 \pm 0.70 \text{ mm a}^{-1}$. For both the total and steric GMSL, we apply the ensemble means presented in WCRP (2018), which are the average of the solutions computed by a number of participating researchers. We also present the mass contributions to sea level trend from the Greenland Ice Sheet, the Antarctic Ice Sheet (AIS), the Gulf of Alaska, and all other land including the Caspian Sea, and note that our AIS mass change time series is included in and agrees well with the AIS gravimetric comparisons presented by Shepherd et al. (2018). The provided regional trend contributions do not exactly sum to the total ocean mass value provided for several reasons: The ocean total includes the restored AOD model which is nonzero over the ocean, we have excluded contributions from the Mediterranean, Black, and Red Seas and Hudson Bay, and we have selected the IJ05_R2 GIA model with a revised ice loading history (Ivins et al. 2013) for AIS to be consistent with the results presented in Shepherd and Ivins (2012) and Luthcke et al. (2013). Estimated AIS mass trends are particularly sensitive to the selected GIA model (Shepherd et al. 2018). It is also important to note that due to the relatively short data record, the reported trend estimates are somewhat sensitive to the selected beginning and end dates. Examination of the GRACE-related uncertainty values in Table 4

Table 4 Trends and uncertainties for 2005.0–2016.0 are listed for the global ocean mass with regional contributions (GSFC mascons), the steric component (WCRP 2018), and the total global mean sea level (GMSL) from the merged satellite altimetry solution (WCRP 2018)

	Trend	Error components			
		Fit	Stoch ^a	Leak ^b	Total
Regional mass					
Global ocean	2.38	0.17	0.03	0.07	0.19
Greenland I.S.	0.84	0.04	0.02	0.02	0.05
Antarctic I.S. ^c	0.36	0.02	0.01	0.02	0.03
Gulf of Alaska	0.17	0.04	0.01	0.00	0.04
Land/Caspian	0.50	0.12	0.06	0.07	0.15
GMSL components					
GMSL (total)	3.70	–	–	–	0.70
Steric	1.31	–	–	–	0.40
Mass + steric ^d	3.69	–	–	–	0.44

The major regional contributions to the ocean mass trends are computed separately. All results apply the AG and Zhong (2013) GIA model correction, except for the Antarctic Ice Sheet which uses IJ05_R2 (Ivins et al. 2013) to follow results presented in Shepherd and Ivins (2012). The 95% uncertainties are provided and all units are mm a^{-1} . The total mass trend errors are the root sum square (RSS) of all error components

^aEqual to $2(\hat{\ell}_\sigma + \bar{\sigma})/\sqrt{(n/z)}$ from Eq. 24

^bEqual to $\hat{\ell}_{\text{trend}}$ from Eq. 24

^cIJ05_R2 GIA applied; 0.61 for (AG and Zhong 2013) GIA

^dSum of global ocean mass and steric; total error is RSS

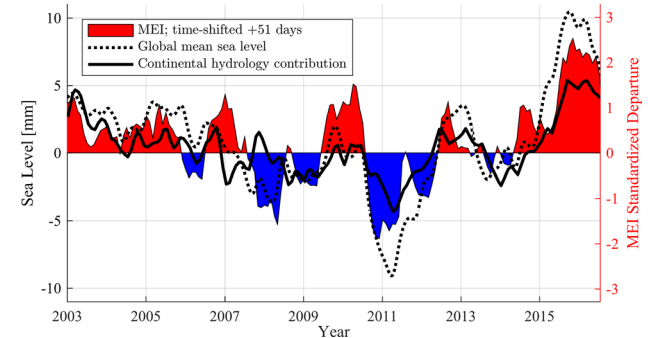


Fig. 12 Comparison between Multivariate ENSO Index (MEI), global mean sea level, and the contribution to global sea level from continental hydrology and glaciers. The sea level signals lag the MEI, so we show the MEI with a time shift of +51 days, which maximizes the correlation between MEI and GMSL

shows that the stochastic and leakage components are small compared to the fit uncertainties. The small leakage errors for the separate constraint regions are not surprising, as one major purpose of the applied regularization is to limit signal leakage across constraint region boundaries (Luthcke et al. 2013).

We conclude with a brief discussion of the interannual variations of GMSL and the relation to the well-known El Niño–Southern Oscillation (ENSO), the most influential climate pattern used in seasonal forecasting. A useful index for

quantifying ENSO is the Multivariate ENSO Index (MEI), which is determined from observations of sea level pressure, surface winds, sea surface temperature, surface air temperature, and cloud cover in the tropical Pacific Ocean. Figure 12 shows the MEI and the de-trended GMSL and ocean mass signals. The high correlation between GMSL and ENSO has been noted by multiple researchers (e.g., Nerem et al. 2010; Cazenave et al. 2012), and the time lag of the GRACE-observed mass change relative to ENSO is discussed by Phillips et al. (2012). We determine that a time lag of 51 days maximizes the correlation between the MEI and GMSL time series, and the MEI in Fig. 12 has been time-shifted accordingly. We compute the following correlation coefficients for the time-shifted MEI: 0.83 for GMSL; 0.68 for GSFC mascon land (including Gulf of Alaska and Caspian Sea); -0.02 for the Greenland Ice Sheet; 0.27 for the Antarctic Ice Sheet. To summarize, the interannual variability in GMSL is largely explained by ENSO, and a significant portion of that interannual GMSL variability is due to terrestrial water storage changes over land, with little input from the large ice sheets whose large contribution is to the GMSL trend.

4 Conclusions

We have presented a novel approach to iteratively solve for mass change anomalies from GRACE Level 1B data, by applying the range-acceleration residuals in the construction of the monthly regularization matrices. This data-driven procedure seeks to minimize the influence of the regularization design on the final solution of this nonlinear estimation problem. The estimation of arc-specific parameters and regularized mascons is highly nonlinear, and we argue that it should be solved iteratively. The original iterative GSFC mascon estimation processing in Luthcke et al. (2013) applied nonlinear constrained least squares, while here we have adopted a new approach in order to leverage the useful information available in the Level 1B residuals.

We have also presented a new and thorough uncertainty assessment of the latest mascon solution, and have argued that regularized geophysical inversion problems are likely to produce biased solutions, and that this bias should be considered when defining solution uncertainties. This bias, or leakage, has been computed here with the full resolution operator, and we have demonstrated the accuracy of this approach with a simulated test case. The noise and leakage uncertainties are now provided with the GSFC mascon products so that end users can easily assign accurate uncertainties for both individual mascons and regions of interest, where both cases have been validated in comparison with independent mascon solutions and calibrated Stokes coefficient uncertainties. Including leakage errors with the mascon product is particularly important, as it is a major error source for

GRACE time-variable gravity solutions, is difficult to compute, and is frequently ignored. With the widespread adoption of GRACE solutions, and the launch of GRACE-FO, it is critically important that time-variable gravity products be properly interpreted, especially with regard to the parameter uncertainties. The detailed uncertainty analysis presented here should clarify both the usefulness and inherent limitations of GRACE products.

Lastly, we have demonstrated the quality of the new GSFC mascon solution by presenting high-resolution global maps of the trend and annual amplitudes, where we have applied the new uncertainties toward the identification of fits with statistical significance. We also presented the successful closure of the global mean sea level budget, when accounting for uncertainties, and noted that for individual constraint regions (e.g., the ocean) that the leakage errors are very small.

Acknowledgements Support for this work was provided by the NASA GRACE and GRACE Follow-On Science Team Grant NNH15ZDA0-01N. We acknowledge the quality of the GRACE Level-1B products produced by our colleagues at the Jet Propulsion Laboratory. We also acknowledge the numerous contributions of D.D. Rowlands, K.E. Rachlin, and J.B. Nicholas in developing the algorithms and software necessary to carry out this research, and we thank the three anonymous reviewers and the editors who provided valuable feedback toward improving this manuscript. The MEI is provided at <https://www.esrl.noaa.gov/psd/enso/mei/>.

A Least-squares and statistical assumptions

A.1 Introduction

Linear least-squares parameter estimation and error assessment typically rely on a set of statistical assumptions that may not be valid. Here, we examine the effect of the assumed statistical properties of the linear system of equations on the bias and covariance of the least-squares state estimator, $\hat{\mathbf{x}}$. We are specifically interested in the properties of the a priori state equation, which we show defines the bias of the estimator, and must be accounted for when assessing the error of the mascon parameters.

We begin by defining linear system of equations for the assumed and truth cases:

$$\begin{aligned}
 \text{costfunction : } & J(\mathbf{x}) = \mathbf{v}^T \mathbf{W} \mathbf{v} + \eta^T \mathbf{P} \eta \\
 \text{assumed : } & \begin{cases} \mathbf{d} = \mathbf{A} \mathbf{x} + \mathbf{v}, \mathbf{v} \sim \mathcal{N}(0, \mathbf{W}^{-1}) \\ \mathbf{x}_a = \mathbf{x} + \boldsymbol{\eta}, \boldsymbol{\eta} \sim \mathcal{N}(0, \mathbf{P}^{-1}) \end{cases} \\
 \text{truth : } & \begin{cases} \mathbf{d} = \mathbf{A} \mathbf{x} + \boldsymbol{\zeta}, \boldsymbol{\zeta} \sim \mathcal{N}(0, \mathbf{R}^{-1}) \\ \mathbf{x}_m = \mathbf{x} + \boldsymbol{\epsilon}, \boldsymbol{\epsilon} \sim \mathcal{N}(0, \mathbf{Q}^{-1}), \end{cases}
 \end{aligned} \tag{A.1}$$

where J is the least-squares cost function to be minimized by the parameters of interest \mathbf{x} , \mathbf{d} is the data vector, \mathbf{A} is the design matrix, \mathbf{x}_a is the a priori best estimate of the true mean state \mathbf{x}_m of \mathbf{x} , and \mathbf{W}^{-1} , \mathbf{R}^{-1} , \mathbf{P}^{-1} , and \mathbf{Q}^{-1} are the covari-

ance matrices of the various zero-mean errors ν , ζ , η , and ϵ , respectively. The errors in statistical information considered here arise in the a priori information as misspecifications in the mean and covariance of the distribution of \mathbf{x} , that is, the difference between \mathbf{x}_a and \mathbf{x}_m and the difference between \mathbf{P} and \mathbf{Q} , respectively, and misspecification in the covariance of the data noise, that is, the difference between \mathbf{W} and \mathbf{R} . The least-squares minimizer of J for the assumed statistical information is given by:

$$\hat{\mathbf{x}} = (\mathbf{A}^T \mathbf{W} \mathbf{A} + \mathbf{P})^{-1} (\mathbf{A}^T \mathbf{W} \mathbf{d} + \mathbf{P} \mathbf{x}_a). \quad (\text{A.2})$$

A.2 The dispersion matrix and mean squared error

The stochastic processes considered here are assumed second-order stationary, and thus, are completely explained by their mean and covariance. For a vector stochastic process \mathbf{z} , these are related by considering the expected value of the total variation, or dispersion, between all pairs of elements, which can be assembled into a dispersion matrix \mathbf{D}_z that can be decomposed as follows:

$$\begin{aligned} \mathbf{D}_z &= \mathbb{E} [\mathbf{z} \mathbf{z}^T] \\ &= \mathbb{E} [(\mathbf{z} - \mathbb{E}[\mathbf{z}] + \mathbb{E}[\mathbf{z}])(\mathbf{z} - \mathbb{E}[\mathbf{z}] + \mathbb{E}[\mathbf{z}])^T] \\ &= \mathbb{E} [(\mathbf{z} - \mathbb{E}[\mathbf{z}])(\mathbf{z} - \mathbb{E}[\mathbf{z}])^T] + \mathbb{E} [\mathbb{E}[\mathbf{z}]\mathbb{E}[\mathbf{z}]^T] \\ &= \mathbf{C}_z + \mathbf{z}_m \mathbf{z}_m^T, \end{aligned} \quad (\text{A.3})$$

where $\mathbb{E}[\cdot]$ is the expectation operator, \mathbf{C}_z is the covariance matrix of \mathbf{z} , and $\mathbf{z}_m = \mathbb{E}[\mathbf{z}]$ is the mean vector.

The mean squared error (MSE) of the estimate is then defined as follows:

$$\begin{aligned} MSE(\hat{\mathbf{x}}) &= \mathbb{E} [(\hat{\mathbf{x}} - \mathbf{x})^T (\hat{\mathbf{x}} - \mathbf{x})] \\ &= Tr \left[\mathbb{E} [(\hat{\mathbf{x}} - \mathbf{x})(\hat{\mathbf{x}} - \mathbf{x})^T] \right] \\ &= Tr[\mathbf{D}_{\hat{\mathbf{x}}-\mathbf{x}}] \\ &= Tr[\mathbf{C}_{\hat{\mathbf{x}}-\mathbf{x}}] + \mathbf{b}^T \mathbf{b}, \end{aligned} \quad (\text{A.4})$$

where $Tr[\cdot]$ is the trace operator and $\mathbf{b} = \mathbb{E}[\hat{\mathbf{x}} - \mathbf{x}]$ is the estimate bias vector. Therefore, we see that the error-covariance matrix $\mathbf{C}_{\hat{\mathbf{x}}-\mathbf{x}}$ and bias vector \mathbf{b} completely define the discrepancy between $\hat{\mathbf{x}}$ and \mathbf{x} .

A.3 Error covariance and bias

We now rewrite the true statistics of the underlying true state \mathbf{x} as:

$$\begin{aligned} \mathbf{x}_m &= \mathbf{x} + \epsilon \\ \mathbf{x}_a &= \mathbf{x} + \mathbf{x}_b + \epsilon, \end{aligned} \quad (\text{A.5})$$

where $\mathbf{x}_b = \mathbf{x}_a - \mathbf{x}_m$, and substitute this and $\mathbf{d} = \mathbf{A} \mathbf{x} + \zeta$ into A.2 such that

$$\hat{\mathbf{x}} = (\mathbf{A}^T \mathbf{W} \mathbf{A} + \mathbf{P})^{-1} (\mathbf{A}^T \mathbf{W} \mathbf{A} \mathbf{x} + \mathbf{A}^T \mathbf{W} \zeta + \mathbf{P} \mathbf{x} + \mathbf{P} \mathbf{x}_b + \mathbf{P} \epsilon). \quad (\text{A.6})$$

The error may now be written as

$$\hat{\mathbf{x}} - \mathbf{x} = (\mathbf{A}^T \mathbf{W} \mathbf{A} + \mathbf{P})^{-1} (\mathbf{A}^T \mathbf{W} \zeta + \mathbf{P} \mathbf{x}_b + \mathbf{P} \epsilon), \quad (\text{A.7})$$

whose expected value, or bias \mathbf{b} , is

$$\mathbb{E} [\hat{\mathbf{x}} - \mathbf{x}] = (\mathbf{A}^T \mathbf{W} \mathbf{A} + \mathbf{P})^{-1} \mathbf{P} \mathbf{x}_b. \quad (\text{A.8})$$

If we define the a priori value of \mathbf{x}_a to be zero, as is the case for GSFC mascon estimation, then this can be rewritten as

$$\begin{aligned} \mathbb{E} [\hat{\mathbf{x}} - \mathbf{x}] &= -(\mathbf{A}^T \mathbf{W} \mathbf{A} + \mathbf{P})^{-1} \mathbf{P} \mathbf{x}_m \\ &= (\mathbf{R} - \mathbf{I}) \mathbf{x}_m, \end{aligned} \quad (\text{A.9})$$

where \mathbf{R} is the resolution operator defined in Eq. 18. As previously noted, the solution bias of Eq. A.9 matches the ridge regression bias presented by (Hoerl and Kennard 1970). To derive the covariance, we note that

$$\hat{\mathbf{x}} - \mathbf{x} - \mathbb{E} [\hat{\mathbf{x}} - \mathbf{x}] = (\mathbf{A}^T \mathbf{W} \mathbf{A} + \mathbf{P})^{-1} (\mathbf{A}^T \mathbf{W} \zeta + \mathbf{P} \epsilon), \quad (\text{A.10})$$

which leads to

$$\begin{aligned} \mathbf{C}'_{\hat{\mathbf{x}}-\mathbf{x}} &= (\mathbf{A}^T \mathbf{W} \mathbf{A} + \mathbf{P})^{-1} (\mathbf{A}^T \mathbf{W} \mathbf{R}^{-1} \mathbf{W} \mathbf{A} + \mathbf{P} \mathbf{Q}^{-1} \mathbf{P}) \\ &\quad (\mathbf{A}^T \mathbf{W} \mathbf{A} + \mathbf{P})^{-1}, \end{aligned} \quad (\text{A.11})$$

where it has been assumed that $\mathbb{E}[\zeta \epsilon^T] = 0$.

To conclude, we observe in Eqs. A.9 and A.11 the effect of invalid statistical assumptions on the bias and covariance, respectively. If the covariance statistics are assumed to be valid, that is, $\mathbf{W} = \mathbf{R}$ and $\mathbf{P} = \mathbf{Q}$, then Eq. A.11 reduces to the familiar form:

$$\mathbf{C}_{\hat{\mathbf{x}}-\mathbf{x}} = (\mathbf{A}^T \mathbf{W} \mathbf{A} + \mathbf{P})^{-1}. \quad (\text{A.12})$$

It can be shown that $\mathbf{C}'_{\hat{\mathbf{x}}-\mathbf{x}} > \mathbf{C}_{\hat{\mathbf{x}}-\mathbf{x}}$, which indicates that this difference in symmetric positive-definite matrices is itself a symmetric positive-definite matrix, that is, it has positive eigenvalues. This means that any variance produced through covariance propagation will be larger for $\mathbf{C}'_{\hat{\mathbf{x}}-\mathbf{x}}$ than the corresponding variance produced by $\mathbf{C}_{\hat{\mathbf{x}}-\mathbf{x}}$.

References

- AG WJ, Zhong S (2013) Computations of the viscoelastic response of a 3-D compressible Earth to surface loading: an application to Glacial Isostatic Adjustment in Antarctica and Canada. *Geophys J Int* 192(2):557–572. <https://doi.org/10.1093/gji/ggs030>
- Carrère L, Lyard F (2003) Modeling the barotropic response of the global ocean to atmospheric wind and pressure forcing—comparisons with observations. *Geophys Res Lett* 30(6):1275–1278. <https://doi.org/10.1029/2002G016473>
- Cazenave A, Henry O, Munier S et al (2012) Estimating ENSO Influence on the Global Mean Sea Level, 1993–2010. *Mar Geodesy* 35:82–97. <https://doi.org/10.1080/01490419.2012.718209>
- Cheng MK, Tapley BD, Ries JC (2013) Deceleration in the Earth's oblateness. *J Geophys Res* 118:1–8. <https://doi.org/10.1002/jgrb.50058>
- Donoho DL, Johnstone IM (1994) Ideal spatial adaptation by wavelet shrinkage. *Biometrika* 81(3):425–455. <https://doi.org/10.1093/biomet/81.3.425>
- Foster M (1961) An application of the Wiener–Kolmogorov smoothing theory to matrix inversion. *J Soc Ind Appl Math* 9(3):387–392. <https://doi.org/10.1137/0109031>
- Hoerl A, Kennard R (1970) Ridge regression: biased estimation for nonorthogonal problems. *Technometrics* 12(1):55–67. <https://doi.org/10.2307/1267351>
- Ivins ER, James TS, Wahr J, Schrama EJO, Landerer FW, Simon KM (2013) Antarctic contribution to sea level rise observed by GRACE with improved GIA correction. *J Geophys Res Solid Earth* 118:3126–3141. <https://doi.org/10.1002/jgrb.50208>
- Kim JR (2000) Simulation study of a low-low satellite-to-satellite tracking mission. Ph.D. thesis, University of Texas at Austin
- Kusche J (2003) Noise variance estimation and optimal weight determination for GOCE gravity recovery. *Adv Geosci* 1:81–85. <https://doi.org/10.5194/adgeo-1-81-2003>
- Kusche J, Springer A (2017) Parameter estimation for satellite gravity field modeling. In: Naeimi M, Flury J (eds) *Global gravity field modeling from satellite-to-satellite tracking data. Lecture notes in Earth system sciences*. Springer, Berlin, pp 127–160. https://doi.org/10.1007/978-3-319-49941-3_4
- Lee J, Lund R (2004) Revisiting simple linear regression with auto-correlated errors. *Biometrika* 91(1):240–245. <https://doi.org/10.1093/biomet/91.1.240>
- Lemoine FG, Goosens S, Sabaka TJ et al (2013) High-degree gravity models from GRAIL primary mission data. *J Geophys Res Planets* 118:1676?1698. <https://doi.org/10.1002/jgre.20118>
- Leuliette E, Willis J (2011) Balancing the sea level budget. *Oceanography* 24(2):122–129. <https://doi.org/10.5670/oceanog.2011.32>
- Loomis BD, Luthcke SB (2014) Optimized signal denoising and adaptive estimation of seasonal timing and mass balance from simulated GRACE-like regional mass variations. *Adv Adapt Data Anal* 06:1450003. <https://doi.org/10.1142/S1793536914500034>
- Loomis BD, Luthcke SB (2017) Mass evolution of Mediterranean, Black, Red, and Caspian Seas from GRACE and altimetry: accuracy assessment and solution calibration. *J Geod* 91(2):195–206. <https://doi.org/10.1007/s00190-016-0952-3>
- Luthcke SB, Zwally HJ, Abdalati W, Rowlands DD, Ray RD, Nerem RS, Lemoine FG, McCarthy JJ, Chinn DS (2006) Recent Greenland ice mass loss by drainage system from satellite gravity observations. *Science* 314(5803):1286–1289. <https://doi.org/10.1126/science.1130776>
- Luthcke SB, Arendt AA, Rowlands DD, McCarthy JJ, Larsen CF (2008) Recent glacier mass changes in the Gulf of Alaska region from GRACE mascon solutions. *J Glaciol* 54(188):767–777. <https://doi.org/10.3189/002214308787779933>
- Luthcke SB, Sabaka TJ, Loomis BD, Arendt AA, McCarthy JJ, Camp J (2013) Antarctica, Greenland and Gulf of Alaska land ice evolution from an iterated GRACE global mascon solution. *J Glaciol* 59(216):613–631. <https://doi.org/10.3189/2013JoG12J147>
- Menke W (2015) Review of the generalized least squares method. *Surv Geophys* 36:1–25. <https://doi.org/10.1007/s10712-014-9303-1>
- Nerem RS, Chambers DP, Choe C, Mitchum GT (2010) Estimating mean sea level change from the TOPEX and Jason altimeter missions. *Mar Geodesy* 33(1):435–446. <https://doi.org/10.1080/01490419.2010.491031>
- Pavlis NK, Holmes SA, Kenyon SC, Factor JK (2012) The development and evaluation of the Earth Gravitational Model 2008 (EGM2008). *J Geophys Res* 117:B04406. <https://doi.org/10.1029/2011JB008916>
- Peltier WR, Argus DF, Drummond R (2015) Space geodesy constrains ice-age terminal deglaciation: the global ICE-6G C (VM5a) model. *J Geophys Res Solid Earth* 120:450–487. <https://doi.org/10.1002/2014JB011176>
- Phillips T, Nerem RS, Fox-Kemper B, Famiglietti JS, Rajagopala B (2012) The influence of ENSO on global terrestrial water storage using GRACE. *Geophys Res Lett* 39:L16705. <https://doi.org/10.1029/2012GL052495>
- Reager JT, Gardner AS, Famiglietti JS, Wiese DN, Eicker A, Lo MH (2016) A decade of sea level rise slowed by climate-driven hydrology. *Science* 351:699–703. <https://doi.org/10.1126/science.aad8386>
- Rodell M, Famiglietti JS, Wiese DN, Reager JT, Beaulieu HK, Landerer FW, Lo MH (2018) Emerging trends in global freshwater availability. *Nature* 557(7707):651–659. <https://doi.org/10.1038/s41586-018-0123-1>
- Rowlands DD, Ray RD, Chinn DS, Lemoine FG (2002) Short-arc analysis of intersatellite tracking data in a gravity mapping mission. *J Geod* 76:307. <https://doi.org/10.1007/s00190-002-0255-8>
- Rowlands DD, Luthcke SB, Klosko S, Lemoine FG, Chinn DS, McCarthy JJ, Cox CM, Anderson OB (2005) Resolving mass flux at high spatial and temporal resolution using GRACE intersatellite measurements. *Geophys Res Lett* 32:L04310. <https://doi.org/10.1029/2004GL021908>
- Rowlands DD, Luthcke SB, McCarthy JJ, Klosko SM, Chinn DS, Lemoine FG, Boy J-P, Sabaka TJ (2010) Global mass flux solutions from GRACE: a comparison of parameter estimation strategies - mass concentrations versus Stokes coefficients. *J Geophys Res* 115:B01403. <https://doi.org/10.1029/2009JB006546>
- Sabaka TJ, Rowlands DD, Luthcke SB, Boy J-P (2010) Improving global mass flux solutions from Gravity Recovery and Climate Experiment (GRACE) through forward modeling and continuous time correlation. *J Geophys Res* 115:B11403. <https://doi.org/10.1029/2010JB007533>
- Save H, Bettadpur S, Tapley BD (2016) High resolution CSR GRACE RL05 mascons. *J Geophys Res Solid Earth* 121:7547–7569. <https://doi.org/10.1002/2016JB013007>
- Savitzky A, Golay MJE (1964) Smoothing and differentiation of data by simplified least squares procedures. *Anal Chem* 36(8):1627–39. <https://doi.org/10.1021/ac60214a047>
- Scanlon BR, Zhang Z, Save H et al (2018) Global models underestimate large decadal declining and rising water storage trends relative to GRACE satellite data. *PNAS*. <https://doi.org/10.1073/pnas.1704665115>
- Shepherd A, Ivins ER et al (2012) A reconciled estimate of ice-sheet mass balance. *Science* 338(6111):1183–1189. <https://doi.org/10.1126/science.1228102>
- Shepherd A et al (2018) Mass balance of the Antarctic Ice Sheet from 1992 to 2017. *Nature* 558(7709):219–222. <https://doi.org/10.1038/s41586-018-0179-y>

- Swenson S, Chambers D, Wahr J (2008) Estimating geocenter variations from a combination of GRACE and ocean model output. *J Geophys Res* 113:B08410. <https://doi.org/10.1029/2007JB005338>
- Tikhonov AN (1963) Solution of incorrectly formulated problems and the regularization method. *Sov Math Dokl* 4:1035–1038
- Wahr J, Molenaar M, Bryan F (1998) Time variability of the Earth's gravity field: Hydrological and oceanic effects and their possible detection using GRACE. *J Geophys Res Solid Earth* 103(B12):30,205–30,229. <https://doi.org/10.1029/98JB02844>
- Wahr J, Swenson S, Velicogna I (2006) Accuracy of GRACE mass estimates. *Geophys Res Lett* 33:L06401. <https://doi.org/10.1029/2005GL025305>
- Wahr J, Nerem RS, Bettadpur SV (2015) The pole tide and its effect on GRACE time-variable gravity measurements: implications for estimates of surface mass variations. *J Geophys Res Solid Earth* 120:4597–4615. <https://doi.org/10.1002/2015JB011986>
- Watkins MM, Wiese DN, Yuan D-N, Boening C, Landerer FW (2015) Improved methods for observing Earth's time variable mass distribution with GRACE using spherical cap mascons. *J Geophys Res Solid Earth*. <https://doi.org/10.1002/2014JB011547>
- WCRP Global Sea Level Budget Group (2018) Global sea level budget 1993-present. *Earth Syst Sci Data* 10:1551–1590. <https://doi.org/10.5194/essd-10-1551-2018>
- Weigelt M (2017) The acceleration approach. In: Naeimi M, Flury J (eds) *Global gravity field modeling from satellite-to-satellite tracking data*. Lecture notes in Earth system sciences. Springer, Berlin, pp 127–160. https://doi.org/10.1007/978-3-319-49941-3_4
- Wiese DN, Landerer FW, Watkins MM (2016) Quantifying and reducing leakage errors in the JPL RL05M GRACE mascon solution. *Water Resour Res* 52:7490–7502. <https://doi.org/10.1002/2016WR019344>